Modeling and Optimization of Activated Nanomagnetic Biochar Derived from Oil Palm Trunk Biomass via Response Surface Methodology for the Removal of Malachite Green Dye

Wan Noni Afida Ab Manan
Universiti Malaysia Pahang Al-Sultan Abdullah, Lebuh Persiaran Tun Khalil Yaakob
Ahmad Zamani Ab Halim
ahmadzamani@umpsa.edu.my
Universiti Malaysia Pahang Al-Sultan Abdullah, Lebuh Persiaran Tun Khalil Yaakob

Article

Keywords: adsorption, malachite green, response surface methodology

Posted Date: July 22nd, 2025

DOI: https://doi.org/10.21203/rs.3.rs-7055845/v1

Additional Declarations: No competing interests reported.

Abstract

Organic dye pollution poses a serious environmental threat, and while activated carbon (AC) is commonly used to adsorb these dyes, its effectiveness is often limited by challenges in separation and regeneration. To address this, activated nanomagnetic biochar (ANB) was developed via a coprecipitation method, utilizing oil palm trunk biomass to create a variant called ANBO for removing malachite green (MG) from water. The synthesized ANBO's physical characteristics were examined using scanning electron microscopy (SEM), Brunauer-Emmett-Teller (BET), Fourier transform infrared spectroscopy (FTIR), and X-ray diffraction (XRD) techniques. This study examined the impact of several process variables, including adsorbent dosage (g), time (minutes), and pH, on the percentage of MG eliminated from aqueous solutions, an application of a Box–Behnken design (BBD) with three factors and three levels within the response surface methodology (RSM) framework, ultimately optimizing MG adsorption with ANBO as the adsorbent. Analysis of variance (ANOVA) revealed that adsorbent dosage had the most significant effect (F = 142.16), followed by pH (F = 37.82) and contact time (F = 20.41). The highest removal efficiency was achieved at optimal conditions of 0.08 g of adsorbent, pH 8, and 1 hour. In conclusion, this research supports Sustainable Development Goals 6 (Clean Water and Sanitation) and 3.9, which aim to reduce health risks from hazardous chemicals and pollution by 2030, aligning with the environmental standards set by the local Department of Environment (DOE).

1. Introduction

Dyes are widely employed in numerous industries, such as textiles, paper, plastics, and leather, for the purpose of coloring items (Lei et al., 2015). Annually, more than 1 million tons of textile dye wastewater are produced worldwide, with approximately 30% being released into untreated water bodies (Ewuzie et al., 2022; Lei et al., 2015). These colors present considerable hazards to both environmental integrity and human health, with many associated with allergies, cancer, and mutations (Liu et al., 2022). Malachite green (MG) is a basic dye widely used in aquaculture due to its demonstrated antibacterial and antifungal properties. The dyeing of silk, cotton, paper, wool, and leather is a possible application for it (Das et al., 2024; Yazid et al., 2024). The feeding behaviors and survival of fish may be influenced by decreased fertility, decreased growth rates, and congenital defects caused by low levels of malachite green (Sharma et al., 2024). Consequently, the elimination of these colors from dye effluent prior to release is a critical concern.

A variety of technologies have been implemented in the past to remove MG dye, aiming to deliver a cost-effective and sustainable solution, and have attracted significant attention (Prasad et al., 2024). These procedures can be classified into biological, physical (including adsorption, coagulation-flocculation, and membrane filtering), and chemical (including advanced oxidation processes) categories (Pramanik et al., 2024). In contrast to other methods, the adsorption method represents a notable strategy for treating dye-contaminated wastewater because of the excellent physical and chemical properties of the absorbent (Liu et al., 2022; Pan et al., 2025). It also generates fewer secondary pollutants, has minimal initial costs, and has rather easy design and operation of the treatment equipment (Krishna Murthy et al., 2020).

Activated carbon (AC) serves as a highly effective option for adsorbing dyes from wastewater due to its diverse pore structure, which includes micropores, mesopores, and macropores, along with its substantial specific surface area and adjustable chemical groups (Jawad & Surip, 2022). However, commercial AC is commonly expensive (Gündüz & Bayrak, 2018); alternatively, biomass is widely utilized as an adsorbent for pollutant removal due to its broad functionalities (Krishna Murthy et al., 2020), non-toxicity, low cost, and biodegradability (Gündüz & Bayrak, 2018). Nevertheless, the comparatively lower adsorption efficiency and extended separation time for dye solutions have constrained the practical application of biomass adsorbents (Peng et al., 2020). Therefore, numerous chemical modification methods, including treatments with acids, bases, oxidants, and organic reagents, have been employed to enhance raw biomass by increasing the abundance of functional groups (Krishna Murthy et al., 2020; Peng et al., 2020; Yalvaç & Bayrak, 2020). These modifications serve to create additional binding sites, thereby addressing the limitations encountered in the adsorption process. In addition, magnetically responsive modifications of biomass adsorbents are gaining increased attention because of their enhanced efficiency and ease of separation from dye solutions (Angelova et al., 2016).

Moreover, optimizing process conditions is essential for producing high-quality AC suitable for various environmental and industrial applications (Sakhiya et al., 2023). When executing experimental procedures, it is essential to use a factorial design

with three levels to employ the Box–Behnken design (BBD) in response surface methodology (RSM). According to Abdullah et al. (2021) and Neisan et al. (2023), BD–RSM can be utilized to achieve ideal adsorption conditions while simultaneously reducing the number of tests and the amount of chemicals used. To the authors' knowledge, no inquiry has been conducted to optimize synthetic dye removal through the utilization of activated nanomagnetic biochar generated from oil palm trunks (OPTs). Consequently, throughout this inquiry, OPT was utilized as a raw material for the creation of activated nanomagnetic biochar, also known as ANBO. X-ray diffraction (XRD), scanning electron microscopy (SEM), BET surface area analysis, and Fourier transform infrared spectroscopy (FTIR) were employed as subsequent methods to characterize the biochar. The adsorption capacity of ANBO was assessed by removing malachite green (MG) during the experiment. A full-factorial experimental strategy was employed to optimize the removal of MG using ultraviolet-visible (UV-vis) spectroscopy. The percentage of MG that was removed from aqueous solutions was investigated using ANBO as the adsorbent. The independent factors investigated included the dosage of the adsorbent, the duration of time, and the pH of the solution. To determine the optimal amount of MG removal and investigate the correlations between the independent variables and the removal of MG components, a BBD design was employed.

2. Experimental

2.1 Materials

All of the synthetic chemicals and solvents were purchased from Merck and Sigma Aldrich, and they were utilized as provided, including iron (III) chloride hexahydrate ($FeCl_3.6H_2O$; 99%), iron (II) sulfate heptahydrate ($FeSO_4.7H_2O$), phosphoric acid (80%), sodium hydroxide (NaOH, 2 M) and ethanol (98%).

2.2 Collection and synthesis of adsorbents

The oil palm trunk (OPT) biomass was sourced from the residual waste generated during wood manufacture that the factory intended to dispose of. The biomass was ground and sieved into small particles (size between 200 and 400 μm).

The chemical activation of biochar was conducted according to the method outlined by Dechapanya & Khamwichit (2023), with certain modifications implemented. A 500 mL solution was prepared using 85% V/V phosphoric acid (H_3PO_4). A 2-g sample of finely ground biochar was immersed in 300 mL of pre-prepared H_3PO_4. The biochar was immersed in acid for 24 h. The activated biochar (AB) was subsequently rinsed with distilled water to reach a pH level of 7. The AB was then dried in an oven at 105°C for a period of 24 hours.

The synthesis of ANB was conducted via the chemical coprecipitation method, adhering to the prescribed process. The synthesis of Fe_3O_4 nanoparticles was accomplished through the use of dissolved hydrate compounds, namely $FeCl_3.6H_2O$ and $FeSO_4.7H_2O$. The compounds function as sources of Fe^{3+} and Fe^{2+} ions, with a mass ratio of 2:1 (Subbaiah Munagapati et al., 2022). 2 g of AB was dispersed in 200 mL of distilled water at 80 ℃. After 10 min, 7.8 g of $FeCl_3.6H_2O$ and 3.8 g of $FeSO_4.7H_2O$ were added (Jain et al., 2018). The resulting mixture was heated for 30 minutes at 80 ℃ while maintaining magnetic stirring at 100 rpm. Following the increase of stirring to 1000 rpm, 30 mL of 2 M sodium hydroxide (NaOH) was added dropwise to adjust the pH to a range of 10–11 (Karami et al., 2024). The resulting mixture was heated for 1 h at 80 ℃ while stirring at 100 rpm. The solid was subsequently separated from the solution using a permanent magnet and then washed with 2 L of distilled water and 100 mL of ethanol until the pH approached neutrality. It was then dried at 100 ℃ for 24 h (Dobrzyńska et al., 2022). The magnetic field produced by a permanent magnet was utilized in this deposition process to improve its efficiency (Rubangakene et al., 2023).

2.3 Experimental Design

The percentage of MG removed from an aqueous solution was the response analyzed using a BBD. The three independent variables that influenced the removal of MG from the solution were the adsorbent dosage, represented by X_1 (g), the contact time, represented by X_2 (minutes), and the pH, represented by X_3. The trial edition of the Design Expert 13.0 program was used to generate the experimental design matrix. The range of values for each of the three independent criteria that were taken into consideration in this investigation is presented in Table 1. Table 3 presents the actual and coded levels of the independent variables employed in the experimental design.

Table 1
Independent variables and their corresponding MG removal efficiencies for ANBO adsorption

Variables	Units	Codes	-1	0	+ 1
Dosage	g	A	0.02	0.05	0.08
Time	min	B	30	60	90
pH		C	6	7	8

All tests were carried out in a randomized manner to minimize the influence of systematic errors on the observed results. The BBD model, based on the second-order polynomial regression indicated in Eq. (1), was employed to demonstrate the correlation among the dependent variable and the operational independent variables.

$$\gamma = \beta_0 + \sum_{i=1}^{n} \beta_i X_i + \sum_{i=1}^{n} X \beta_{ii} X_i^2 + \sum_{i=1}^{n} \sum_{i=j}^{n} \beta ij X_i X_j + t \quad \text{Eq. (1)}$$

Where γ represents the projected response (MG removal), β_0, β_{ii}, and β_{ij} represent the linear, quadratic, and interaction coefficients, respectively, X_i and X_{ij} representing the input coded and independent variables, and t representing the residual error (El-Sharkawy et al., 2024).

To determine the validity of the model, an analysis of variance (ANOVA) was conducted. This allowed for the evaluation of the correlation between the response and the process variables following the suggested model. To determine whether the model was statistically significant, both the Fisher *F*-distribution test and the *p*-value were utilized simultaneously (Abdullah et al., 2021; Zamani & Abdullah, 2018).

2.4 Characterization

A series of 50 mL NaCl solutions was mixed with 0.10 g of ANBO to determine the zero-point charge pH (pHzpc). The initial pH range was between 2 and 10. To achieve this pH, 0.1 M NaOH or HCl was used. After a 24-hour period, the pH of each filtrate was determined using a pH meter that had been calibrated (Milwaukee 150). To evaluate the surface morphology of ANBO, a scanning electron microscope (SEM-EDX, TESCAN VEGA3) equipped with an energy-dispersive X-ray analyzer was utilized. Analyses of the synthesized functional groups of the ANBO were accomplished using an FTIR spectrometer with a wavenumber range of 400 to 4000 cm^{-1}, mounted on a PerkinElmer infrared spectrometer equipped with an attenuated total reflection (ATR) accessory. To determine the surface area of the ANBO, a Brunauer-Emmett-Teller (BET) analyzer, specifically a Micromeritics TriStar II Plus, was used. To investigate the phase purity and crystalline characteristics of the ANBO synthesized, powder X-ray diffraction (XRD) was employed. To conduct this investigation, a PAN analytical apparatus was used, employing a Cu-Kα radiation probe beam with a wavelength of 1.54056 Å. Within a temperature range of 10–80°, the sample was analyzed.

2.5 MG adsorption study

8 mg of ANBO were combined with 50 mL of an MG solution that had a concentration of 10 ppm. After that, the mixture was placed in an incubator shaker set to 100 rpm, allowing the contact time to be calculated using RSM based on the optimized value. An external magnet was used to separate the adsorbent once the adsorption process was complete. To determine the adsorption capacity of MG, a UV-Vis spectrophotometer (UV-1800, Shimadzu, Japan) was used, with the maximum wavelength (λ_{max}) set at 617 nm. Both the adsorption capacity (Q_e) and the removal efficiency (R) were calculated using Equations (2) and (3), respectively. (Zhang et al., 2023).

$$Qe = \frac{C_0 - C_e}{m} \times V \quad \text{Eq. (2)}$$

$$R\ (\%) = \frac{C_0 - C_e}{C_O} \times 100 \quad \text{Eq. (3)}$$

3. Results and Discussion

3.1 Zero Point of Charge (pH_{zpc})

When the total surface charge of ANBO is equal to zero, the pH reaches its highest, which is known as the pH_{zpc}. The data in Fig. 1 indicates that ANBO's pH_{zpc} value is 6.3. When the pH falls below 6.3, the ANBO surface maintains its positive charge. However, as the pH rises beyond 6.3, the negatively charged surface of ANBO facilitates the adsorption of the positively charged MG dye through ionic or electrostatic interactions.

3.2 Functional group analysis by FTIR

The FTIR spectra in Fig. 2 display the vibrational bands of the various materials, which were recorded between 4000 and 400 cm^{-1}. Comparing the ANBO spectra pre- and post-adsorption revealed notable differences. The peak, which is roughly 3410 cm^{-1}, is associated with the distinctive stretching vibration of hydroxyl groups. The C = O peak is located at 1585 cm^{-1}, whereas the deformation vibrations of the C = C stretching bonds are responsible for another band at about 1355 cm^{-1}. Because the reaction takes place during the adsorption between ANBO and the MG solution, there are minor variations in the FTIR spectrum for ANBO after adsorption as compared to that before adsorption. The C-H symmetric stretching vibrations and C-H in-plane deformation are represented by the peaks at 1166 cm^{-1} and 904 cm^{-1} (Abdullah et al., 2021). The stretching vibrations of Fe-O bonds were identified as the source of the peak at 564 cm^{-1} (Zhang et al., 2023), indicating the successful synthesis of magnetic properties in ANBO.

3.3 Scanning electron microscopy (SEM) analysis

SEM characterized the form and size of the adsorbents. Figure 2 illustrates the surface morphology of OPT, activated biochar (AB), and ANBO before and after adsorption. A comparison of the microstructure of OPT (Fig. 3(a)) and ABO (Fig. 3(b)) revealed that ABO had higher porosity than OPT. Moreover, a rougher surface with a large number of granular bulges can be observed in ANBO (Fig. 3 (d)). This result suggested that Fe_3O_4 was successfully loaded on the ABO after the magnetization reaction via the coprecipitation method which improved the porosity and number of surface functional groups (Ntinkam Simo et al., 2024; Zhang et al., 2023). After MG adsorption, the surface changed into a more uneven structure (Fig. 3 (e)), indicating that MG was attached to ANBO. The diameter of 100 particles per image was quantified via ImageJ software to analyze the particle size distribution (Karami et al., 2024).

Figure 4 displays the energy dispersive X-ray spectroscopy (EDX) analysis results for ANBO before adsorption. Based on the elemental composition analysis in Fig. 4 (e), the main elements present in ANBO were carbon (C), oxygen (O), and iron (Fe). However, the other elements that were detected in ANBO included calcium (Ca), sodium (Na), and silica (Si), which were not the major elements. The presence of gold (Au) in the spectra was due to its use for sample coating.

Figure 5 shows the EDX analysis results for ANBO after adsorption. This observation indicated that the dye molecules were dispersed uniformly across the ANBO surface. The strong signal from the increase in carbon content after the adsorption of MG dye was attributed to the dye molecules loaded onto the surface of ANBO.

3.4 BET Analysis

Figure 6 illustrates the N_2 adsorption-desorption isotherms of ANBO. Table 2 shows the BET surface area, pore volume, and average pore diameter of ABO and ANBO. Table 2 indicates that ABO possessed a BET surface area of 34.28 m^2/g. Furthermore, the pore volume and size were 0.010 cm^3/g and 12.243 Å, respectively. Upon modification of ABO with Fe_3O_4, the BET surface area was elevated to 76.07 m^2/g in ANBO. The mean pore diameter was 10.378 Å, and there was a notable increase in pore volume to 0.019 cm^3/g. Consequently, the alteration of ABO with Fe_3O_4 significantly enhanced the surface area and pore volume. The enhanced surface area is due to the uniform distribution of iron nanoparticles on the ABO surface. The augmentation of pore volume mostly results from the elimination of contaminants and the expansion of micropores. The results of the current study align with those of Kumar et al. (2023).

Table 2
S_{BET}, pore volume and pore diameter of ABO and ANBO

Materials	S_{BET} (m^2/g)	*Pore volume* (cm^3/g)	*Pore size* (Å)
ABO	34.28	0.010	12.243
ANBO	76.07	0.019	10.378

The N_2 adsorption-desorption isotherm of ANBO (Fig. 6) was type IV, and the hysteresis loop at p/p^0 ranged from 0.4 to 1.0, which confirmed the presence of abundant mesopores (Xiao et al., 2025; Zhang et al., 2023).

3.5 XRD analysis

XRD analysis was used to assess the degree of crystallinity or amorphousness of the samples. Crystalline substances display distinct peaks, whereas noncrystalline or amorphous materials show broad peaks (Ngernyen et al., 2023). The XRD patterns of ABO and ANBO before and after adsorption are shown in Fig. 7. During ABO, activation caused a modification in the diffraction pattern. No distinctive peaks were present in the spectra of ABO, and a broad peak appeared at a diffraction angle 20–30° with corresponding planes of 002, indicating that ABO was not crystalline and possessed an amorphous structure according to JCPDS No. 75–1621 (Jawad & Surip, 2022). The results obtained may be explained by the significant iron deficiency observed, which is consistent with earlier findings. In comparison, multiple sharp peaks were observed in the 2θ range of 20–80° for ANBO before and after adsorption, implying that the degree of crystallinity in the phases present in the ANBOs. X-ray diffraction of ANBO after adsorption at 30.2°, 35.6°, 43.3°, 57.2° and 62.9° can be observed, which is related to diffraction from planes (220), (311), (511), (400), and (440) of magnetite (ICCD 005-4319) (Rubangakene et al., 2023).

3.6 Box–Behnken (BB) design

Table 3 presents the experimental outcomes obtained through the optimization of MG removal using the BBD, which involved 17 randomly conducted experimental trials. The BB design is a second-order response surface methodology that assesses each variable at three different levels (El-Shafie et al., 2024). Three independent variables (adsorbent dosage, contact time, and pH) were chosen to identify the most significant factors affecting MG removal. The experimental results obtained from the full-factorial BBD were modelled using a quadratic equation through multiple regression analysis. The quadratic model for the elimination of MG (response) as a function of three independent variables is shown in Eq. (4):

$$MG\ removal\ (\gamma) = 91.8 + 11.875A + 4.5B + 6.125C - 1.25AB - 0.5AC - 7.75BC - 12.9A^2 - 6.15B^2 - 1.4C^2$$ Eq. (4)

Where γ is the estimated response (MG removal), and A, B, and C are the independent variables of the adsorbent dosage, contact time, and pH, respectively.

Table 3
Experimental design for ANBO adsorption with independent variables and experimental and predicted values of the response

Run	Adsorbent dosage (A)	Contact time (B)	pH (C)	MG removal (%)	
				Actual	Predicted
1	0.05	30	8	94	93.62
2	0.08	60	6	84	83.75
3	0.02	30	7	55	55.12
4	0.02	60	8	72	72.25
5	0.02	60	6	62	59.00
6	0.08	60	8	92	95.00
7	0.02	90	7	64	66.63
8	0.08	30	7	84	81.37
9	0.05	90	6	90	90.38
10	0.05	60	7	92	91.80
11	0.05	90	8	90	87.13
12	0.08	90	7	88	87.87
13	0.05	30	6	63	65.87
14	0.05	60	7	91	91.80
15	0.05	60	7	93	91.80
16	0.05	60	7	93	91.80
17	0.05	60	7	90	91.80

Table 4 displays the ANOVA findings derived from the established quadratic model for the elimination of MG under the specified experimental conditions. The results of the study indicated statistical validity of the model, as evidenced by the *F*-value of 38.66 and the *p*-value of less than 0.001. With an *F*-value of 142.16, the results reveal that A was the most significant parameter, followed by C with an *F*-value of 37.82. Furthermore, C was the second most significant parameter. Parameter B, with an *F*-value of 20.41, had the least influence. The *p*-value must be less than 0.05 for the model to be declared statistically significant (Abdullah et al., 2021). The lack-of-fit rating calculated was 16.25, indicating that the lack of fit is insignificant compared to the error that would occur solely by chance. There was a statistically significant likelihood of 2.69% that the lack of fit was caused by noise. This indicates that the ANOVA predictive model is in strong alignment in this regard (Zamani & Abdullah, 2018).

Table 4
ANOVA results for MG removal

Source	Sum of Squares	Degree of Freedom	Mean Square	*F*-Value	*P*-Value
Model	2760	9	306	38.66	< 0.0001
A-Dosage	1128.125	1	1128.13	142.16	< 0.0001
B-Time	162.00	1	162.00	20.41	0.0027
C-pH	300.12	1	300.12	37.82	0.0005
AB	6.25	1	6.25	0.7876	0.4043
AC	1.0000	1	1.0000	0.1260	0.7331
BC	240.25	1	240.25	30.27	0.0009
A^2	700.67	1	700.67	88.29	< 0.0001
B^2	159.25	1	159.25	20.07	0.0029
C^2	8.25	1	8.25	1.04	0.3418
Residual	55.55	7	7.94		
Lack of fit	48.75	3	16.25	9.56	0.0269
Pure error	6.80	4	1.70		
Std. Dev.	2.82		R^2	0.9803	
Mean	82.18		Adj R^2	0.9549	
			Predicted R^2	0.7193	

The correlation coefficient of the model quantifies the link between the variables. A number approaching 1 indicates a more robust match. The R^2 score is 0.9803, while the corrected R^2 is 0.9549, demonstrating a strong correlation with the polynomial equation. The model demonstrated considerable prediction and was statistically significant (Ma et al., 2023). Figure 4 illustrates a contrast between the expected and actual percentages of MG eradication. The residual distribution fit plot demonstrates the discrepancy between predicted and experimental values; a reduced degree of residual distribution signifies enhanced model accuracy (Zhang et al., 2023). The experimental analysis and linear models in ANOVA assume that the residuals follow a normal distribution and are independent (Mohammadpour et al., 2023). Figures 8 (a) and (b) corroborate these assumptions, demonstrating the suitability of the selected model for data analysis.

3.7 Response surface plots and Pareto charts

The Pareto chart serves as a tool for evaluating the importance of evaluated variables and their magnitudes, although it does not indicate the direction of these magnitudes (El-Shafie et al., 2024). Figure 9 illustrates the Pareto chart, whereby % R represents the response being optimized (MG dye solutions). Any variable that surpasses the reference line is statistically significant. The examination of the standard effects (exceeding 2.36) derived from the Pareto diagram revealed that the interactions among several factors had a more pronounced impact than the isolated effects of each factor individually (Ntinkam Simo et al., 2024). A comparison of single factors revealed that the reaction dosage was the most influential parameter in terms of MG removal.

Three-dimensional (3D) and two-dimensional (2D) plots were generated to illustrate the correlations between the independent variables (A, B, and C) and the response variable (MG removal), as depicted in Fig. 10. The results revealed that the response surface was convex, indicating that the optimal circumstances were clearly delineated and that each variable possessed a maximum value. Moreover, the contour form may intuitively depict the degree of engagement. The ellipse signifies a substantial interaction between two components, while the circular shape denotes a divergent relationship (Ma et al., 2023). Figure 10 illustrates that the *P*-value for BC (0.0009) was below 0.05, indicating a robust interaction between time and pH, which suggests

that both factors significantly influence MG removal effectiveness, corroborating the findings from the analysis of variance (Table 4). The data in Figs. 10 (a) and (b) are virtually circular, indicating that the interaction between the components was nearly negligible.

The experiment was validated at optimal settings to achieve maximum MG elimination, as presented in Table 5. The findings indicated that the optimal adsorption parameters for MG were as follows: adsorbent dosage = 0.08 g; time = 60 min; pH = 8; and predictive adsorption capacity = 95%. To simplify the practical operation, the adsorbent dosage used in the verification experiments was similar to the optimum condition, 0.08 g, for 1 hour, and the pH was maintained at 8. The verification experiment demonstrated that the MG adsorption value was 91%, with a maximum error of only ± 4.21%. The response surface optimization method is dependable, and the determined optimal conditions provide considerable practical value. (Ma et al., 2023).

Table 5
Values of the process parameters for the maximum percentage of MG removed.

Setup	**Description**	**Optimization**
	Percentage of MG Removal (%)	**is target = 100**
	A (Adsorbent Dosage, g)	**is in range**
	B (Time, min)	**is in range**
	C (pH)	**is in range**
Suggestions	MG Removal (%)	95
	A (Adsorbent Dosage, g)	0.08
	B (Time, min)	60
	C (pH)	8
	Desirability	1.00
Predicted result	MG Removal (%)	95
Actual experimental results	MG Removal (%)	91
	Error (%)	± 4.21

4. Conclusion

This study revealed that ANBO, synthesized from oil palm trunk (OPT), functions effectively as an adsorbent for removing MG dye from aqueous solutions. SEM analysis of the synthesized ANBO revealed a porous architecture with a textured surface, favorable for dye adsorption. FTIR identified the existence of several carbon–carbon, carbon–oxygen, carbon–hydrogen, and Fe-O linkages that likely facilitated the adsorption of dyes onto the surface of ANBO. The adsorption value was optimised using the response surface methodology through the Box–Behnken design. This study investigated the impact of various parameters, including adsorbent dosage, contact duration, and pH, on the adsorption of MG by ANBO. The ANOVA findings demonstrated that a maximum MG removal of 91% was attained under ideal conditions: an adsorbent dosage of 0.08 g, a contact period of 60 minutes, and a pH of 8. The verification experiment performed under ideal conditions revealed that the experimental MG clearance rate of 91% nearly matched the predicted rate of 95%. In conclusion, ANBO, derived from biomass waste, is a promising and economical adsorbent for removing pollutants from aqueous solutions.

Declarations

8. Conflict of interest

According to the authors, there are no conflicts of interest.

7. Funding

Under the Skim Latihan Akademik Bumiputera (SLAB) initiative, the Ministry of Higher Education in Malaysia is providing financial assistance to this research project.

Author Contribution

Wan Noni Afida Ab Manan (Conceptualization; Formal analysis; Visualization; Writing - original draft; Resources); Ahmad Zamani Ab Halim (Supervision; Writing – review and editing). All the authors have read and agreed to the published version of the manuscript.

Acknowledgement

The authors would like to acknowledge with gratitude the financial support from the Ministry of Higher Education, Malaysia, under the Skim Latihan Akademik Bumiputera (SLAB). The authors would also like to acknowledge the services and facilities provided by UiTM Pahang Branch and Universiti Malaysia Pahang Al-Sultan Abdullah to carry out the laboratory work.

Data Availability

The authors declare that the data supporting the findings of this study are accessible within the paper. Raw data files in alternative formats can be obtained from the corresponding author, Dr. Ahmad Zamani Ab Halim, upon reasonable request.

References

1. Abdullah, N. H., Mohamed, M., Shohaimi, N. A. M., Lazim, A. M., Halim, A. Z. A., Shukri, N. M., & Khairul Azhar Abdul Razab, M. (2021). Enhancing the Decolorization of Methylene Blue Using a. *Molecules*.
2. Angelova, R., Baldikova, E., Pospiskova, K., Maderova, Z., Safarikova, M., & Safarik, I. (2016). Magnetically modified Sargassum horneri biomass as an adsorbent for organic dye removal. *Journal of Cleaner Production*, *137*, 189–194. https://doi.org/10.1016/j.jclepro.2016.07.068
3. Das, T., Debnath, A., & Manna, M. S. (2024). Adsorption of malachite green by Aegle marmelos-derived activated biochar: Novelty assessment through phytotoxicity tests and economic analysis. *Journal of the Indian Chemical Society*, *101*(9), 101219. https://doi.org/10.1016/j.jics.2024.101219
4. Dechapanya, W., & Khamwichit, A. (2023). Biosorption of aqueous Pb(II) by H3PO4-activated biochar prepared from palm kernel shells (PKS). *Heliyon*, *9*(7). https://doi.org/10.1016/j.heliyon.2023.e17250
5. Dobrzyńska, J., Wysokińska, A., & Olchowski, R. (2022). Raspberry stalks-derived biochar, magnetic biochar and urea modified magnetic biochar - Synthesis, characterization and application for As(V) and Cr(VI) removal from river water. *Journal of Environmental Management*, *316*. https://doi.org/10.1016/j.jenvman.2022.115260
6. El-Shafie, A. S., Rahman, E., GadelHak, Y., Mahmoud, R., & El-Azazy, M. (2024). Techno-economic assessment of waste mandarin biochar as a green adsorbent for binary dye wastewater effluents of methylene blue and basic fuchsin: Lab- and large-scale investigations. *Spectrochimica Acta - Part A: Molecular and Biomolecular Spectroscopy*, *306*(May 2023). https://doi.org/10.1016/j.saa.2023.123621
7. El-Sharkawy, R. M., Khairy, M., Zaki, M. E. A., & Abbas, M. H. H. (2024). Innovative optimization for maximum magnetic nanoparticles production by Trichoderma asperellum with evaluation of their antibacterial activity, and application in sustainable dye decolorization. *Environmental Technology and Innovation*, *35*(May), 103660. https://doi.org/10.1016/j.eti.2024.103660
8. Ewuzie, U., Saliu, O. D., Dulta, K., Ogunniyi, S., Bajeh, A. O., Iwuozor, K. O., & Ighalo, J. O. (2022). A review on treatment technologies for printing and dyeing wastewater (PDW). *Journal of Water Process Engineering*, *50*(July), 103273. https://doi.org/10.1016/j.jwpe.2022.103273

9. Gündüz, F., & Bayrak, B. (2018). Synthesis and performance of pomegranate peel-supported zero-valent iron nanoparticles for adsorption of malachite green. *Desalination and Water Treatment*, *110*, 180–192. https://doi.org/10.5004/dwt.2018.22185
10. Jain, M., Yadav, M., Kohout, T., Lahtinen, M., Garg, V. K., & Sillanpää, M. (2018). Development of iron oxide/activated carbon nanoparticle composite for the removal of Cr(VI), Cu(II) and Cd(II) ions from aqueous solution. *Water Resources and Industry*, *20*(October), 54–74. https://doi.org/10.1016/j.wri.2018.10.001
11. Jawad, A. H., & Surip, S. N. (2022). Upgrading low rank coal into mesoporous activated carbon via microwave process for methylene blue dye adsorption: Box Behnken Design and mechanism study. *Diamond and Related Materials*, *127*(May), 109199. https://doi.org/10.1016/j.diamond.2022.109199
12. Karami, N., Mohammadpour, A., Samaei, M. R., Amani, A. M., Dehghani, M., Varma, R. S., & Sahu, J. N. (2024). Green synthesis of sustainable magnetic nanoparticles Fe3O4 and Fe3O4-chitosan derived from Prosopis farcta biomass extract and their performance in the sorption of lead(II). *International Journal of Biological Macromolecules*, *254*. https://doi.org/10.1016/j.ijbiomac.2023.127663
13. Krishna Murthy, T. P., Gowrishankar, B. S., Krishna, R. H., Chandraprabha, M. N., & Mathew, B. B. (2020). Magnetic modification of coffee husk hydrochar for adsorptive removal of methylene blue: Isotherms, kinetics and thermodynamic studies. *Environmental Chemistry and Ecotoxicology*, *2*, 205–212. https://doi.org/10.1016/j.enceco.2020.10.002
14. Kumar, P., Patel, A. K., Singhania, R. R., Chen, C. W., Saratale, R. G., & Dong, C. Di. (2023). Enhanced copper (II) bioremediation from wastewater using nano magnetite (Fe3O4) modified biochar of Ascophyllum nodosum. *Bioresource Technology*, *388*(July), 129654. https://doi.org/10.1016/j.biortech.2023.129654
15. Lei, D. Y., Li, B., Wang, Q., Wu, B., Ma, L., & Xu, H. (2015). Removal of neutral red from aqueous solution using Pleurotus ostreatus nanoparticles by response surface methodology. *Desalination and Water Treatment*, *54*(10), 2794–2805. https://doi.org/10.1080/19443994.2014.904817
16. Liu, Z., Huang, X., Miao, Y., Gao, B., Shi, Y., Zhao, J., & Tan, S. H. (2022). Eggplant biomass based porous carbon for fast and efficient dye adsorption from wastewater. *Industrial Crops and Products*, *187*(PB), 115510. https://doi.org/10.1016/j.indcrop.2022.115510
17. Ma, W., Xu, Y., Zhou, D., Wang, L., Liang, X., & Sun, Y. (2023). *Development and optimization of high – performance nano – biochar for efficient removal Cd in aqueous : Absorption performance*. *189*, 516–529.
18. Mohammadpour, A., Karami, N., Zabihi, R., Fazeliyan, E., Abbasi, A., Karimi, S., Barbosa de Farias, M., Adeodato Vieira, M. G., Shahsavani, E., & Mousavi Khaneghah, A. (2023). Green synthesis, characterization, and application of Fe3O4 nanoparticles for methylene blue removal: RSM optimization, kinetic, isothermal studies, and molecular simulation. *Environmental Research*, *225*(October 2022). https://doi.org/10.1016/j.envres.2023.115507
19. Neisan, R. S., Saady, N. M. C., Bazan, C., Zendehboudi, S., & Albayati, T. M. (2023). Adsorption of copper from water using TiO2-modified activated carbon derived from orange peels and date seeds: Response surface methodology optimization. *Heliyon*, *9*(11). https://doi.org/10.1016/j.heliyon.2023.e21420
20. Ngernyen, Y., Petsri, D., Sribanthao, K., Kongpennit, K., Pinijnam, P., Pedsakul, R., & Hunt, A. J. (2023). Adsorption of the non-steroidal anti-inflammatory drug (ibuprofen) onto biochar and magnetic biochar prepared from chrysanthemum waste of the beverage industry. *RSC Advances*, *13*(21), 14712–14728. https://doi.org/10.1039/d3ra01949g
21. Ntinkam Simo, C. A., Dika Manga, J., & Kede, C. M. (2024). Green synthesis and physicochemical characterization of an eco-friendly zero-valent iron biochar based on Coula edulis shell and morinda bark extract using response surface analysis. *Materials Advances*, *6*, 184–195. https://doi.org/10.1039/d4ma00714j
22. Pan, X., Zhao, N., Shi, H., Wang, H., Ruan, F., Wang, H., & Feng, Q. (2025). Biomass activated carbon derived from golden needle mushroom root for the methylene blue and methyl orange adsorption from wastewater. *Industrial Crops and Products*, *223*(September 2024), 120051. https://doi.org/10.1016/j.indcrop.2024.120051
23. Peng, L., Gao, J., Yao, S., Lan, X., Li, H., & Song, H. (2020). Modified ginkgo leaves for adsorption of methyl violet and malachite green dyes in their aqueous system. *Desalination and Water Treatment*, *206*, 358–370. https://doi.org/10.5004/dwt.2020.26236
24. Pramanik, D. Das, Garg, P., Ganesan, D., & Pramanik, A. (2024). Removal of malachite green from an aqueous environment using chitosan-xanthan gum coagulation system: A response surface methodology approach. *Journal of Water Process*

Engineering, *65*(May), 105896. https://doi.org/10.1016/j.jwpe.2024.105896

25. Prasad, B., Goswami, R., Mishra, A., Gill, F. S., Juyal, S., Asrani, A., Jain, A., Sahu, R., Gupta, M. K., Bajaj, M., & Zaitsev, I. (2024). Assessment of carbonized himalayan chir pine biomass as an eco-friendly adsorbent for effective removal of industrial dyes. *Scientific Reports*, *14*(1), 1–17. https://doi.org/10.1038/s41598-024-66745-z
26. Rubangakene, N. O., Elkady, M., Elwardany, A., Fujii, M., Sekiguchi, H., & Shokry, H. (2023). Effective decontamination of methylene blue from aqueous solutions using novel nanomagnetic biochar from green pea peels. *Environmental Research*, *220*. https://doi.org/10.1016/j.envres.2023.115272
27. Sakhiya, A. K., Kaushal, P., & Vijay, V. K. (2023). Process optimization of rice straw-derived activated biochar and biosorption of heavy metals from drinking water in rural areas. *Applied Surface Science Advances*, *18*(August). https://doi.org/10.1016/j.apsadv.2023.100481
28. Sharma, P., Sharma, S., Sharma, S. K., Yifei, S., Guo, F., Ichikawa, T., Jain, A., & Shrivastava, K. (2024). Evaluation of optimized conditions for the adsorption of malachite green by SnO2-modified sugarcane bagasse biochar nanocomposites. *RSC Advances*, *14*(40), 29201–29214. https://doi.org/10.1039/d4ra05442c
29. Subbaiah Munagapati, V., Wen, H. Y., Gollakota, A. R. K., Wen, J. C., Shu, C. M., Andrew Lin, K. Y., Tian, Z., Wen, J. H., Mallikarjuna Reddy, G., & Zyryanov, G. V. (2022). Magnetic Fe3O4 nanoparticles loaded papaya (Carica papaya L.) seed powder as an effective and recyclable adsorbent material for the separation of anionic azo dye (Congo Red) from liquid phase: Evaluation of adsorption properties. *Journal of Molecular Liquids*, *345*. https://doi.org/10.1016/j.molliq.2021.118255
30. Xiao, X., Zhou, F., Yang, C., Lu, L., Zhao, Y., Tu, B., & Li, L. (2025). Adsorption and reduction of Cr(VI) by C-P-O groups in biochar: Performance and mechanisms. *Solid State Sciences*, *160*(November 2024), 107815. https://doi.org/10.1016/j.solidstatesciences.2024.107815
31. Yalvaç, G. M., & Bayrak, B. (2020). Use of natural and effective mandarin peel in elimination of malachite green from the aqueous media: Adsorption properties, kinetics and thermodynamics. *Desalination and Water Treatment*, *177*, 176–185. https://doi.org/10.5004/dwt.2020.24876
32. Yazid, H., Bouzid, T., Naboulsi, A., Grich, A., el Mountassir, E. M., Regti, A., El Himri, M., & El Haddad, M. (2024). Adsorption of malachite green using waste marine cuttlefish bone powder: Experimental and theoretical investigations. *Marine Pollution Bulletin*, *209*(PB), 117210. https://doi.org/10.1016/j.marpolbul.2024.117210
33. Zamani, A. H., & Abdullah, N. H. (2018). Modeling and optimization of carbon dioxide methanation via in situ hydrogen generated from aluminum foil and alkaline water by Box–Behnken design. *Journal of the Taiwan Institute of Chemical Engineers*, *82*, 156–162. https://doi.org/10.1016/j.jtice.2017.11.013
34. Zhang, L., Wang, Y., Liu, Y., Lv, S., Wang, R., Hu, X., Liu, Y., Dong, Z., Lin, K., & Liu, L. (2023). Chloride removal from sewage using bismuth trioxide: Characterization and optimization by response surface methodology (RSM). *Journal of Environmental Chemical Engineering*, *11*(5). https://doi.org/10.1016/j.jece.2023.110868
35. Zhang, X., Qiu, C., Li, F., Zhang, X., Li, M. C., Xie, J., de Hoop, C. F., Qi, J., & Huang, X. (2023). Magnetic nanocellulose-based adsorbent for highly selective removal of malachite green from mixed dye solution. *International Journal of Biological Macromolecules*, *253*(P2), 126752. https://doi.org/10.1016/j.ijbiomac.2023.126752

Figures

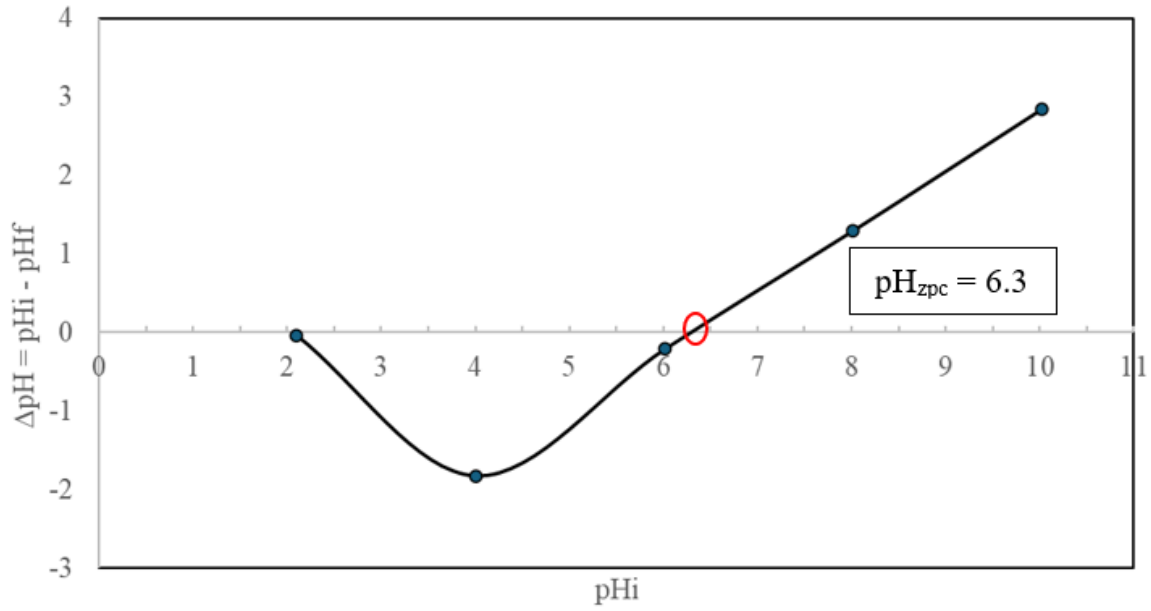

Figure 1

Plot of the pH_{zpc} of ANBO

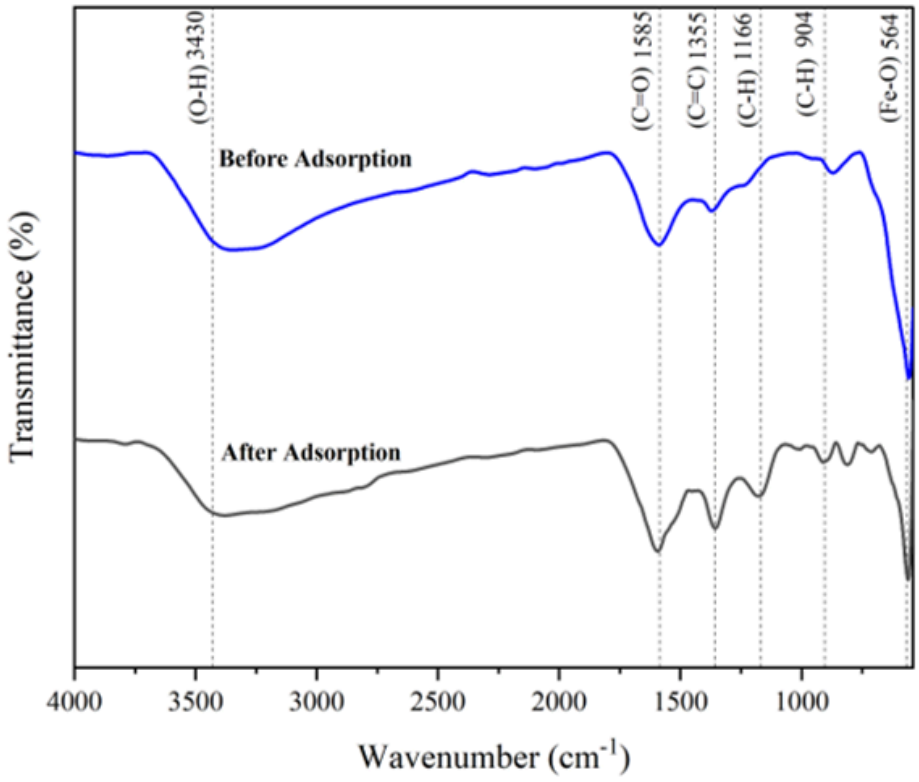

Figure 2

FTIR spectra of ANBO before and after adsorption

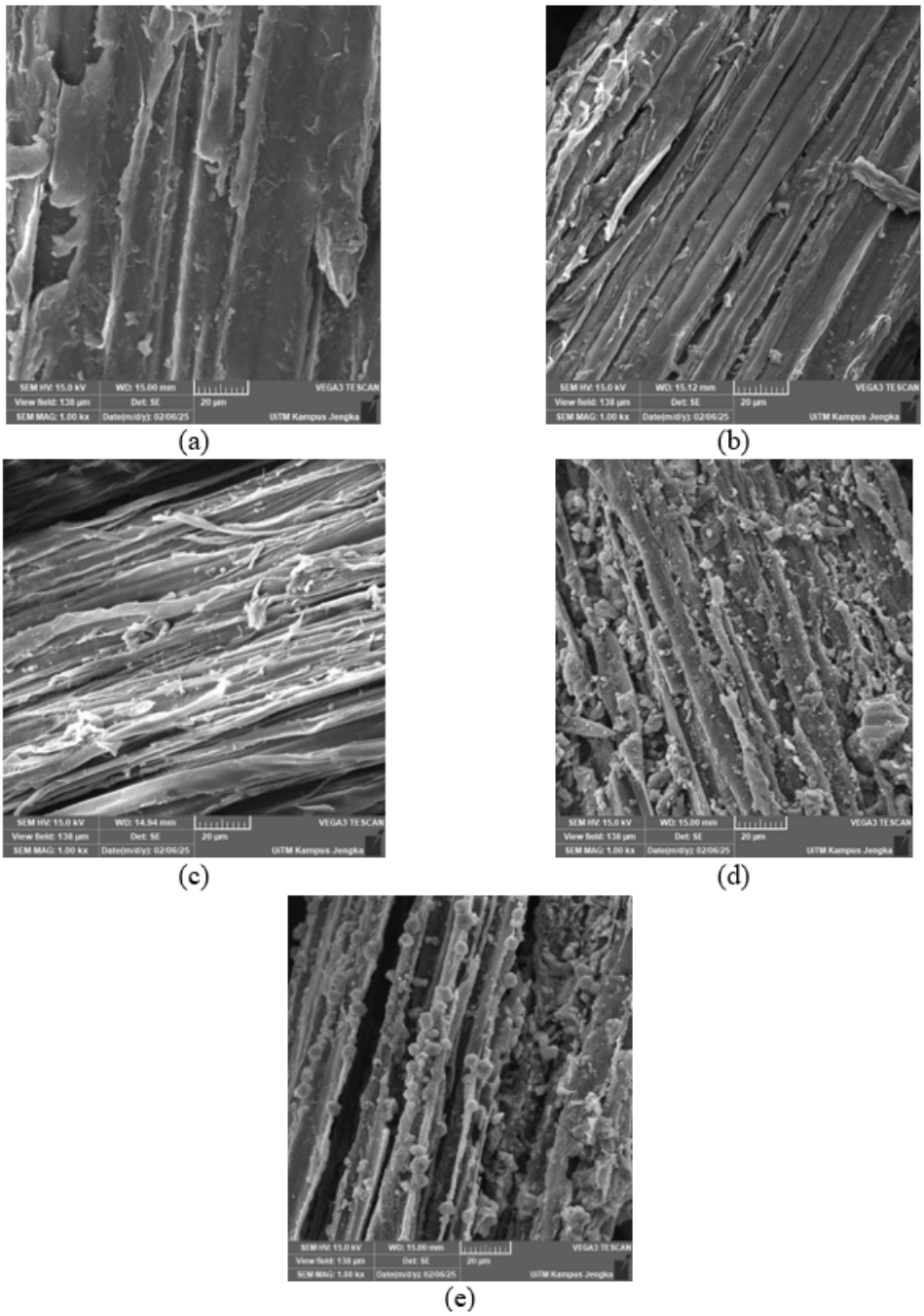

Figure 3

Sem images (magnification = 1000x) of (a) OPT, (b) OPTB, (c) ABO, (d) ANBO Before and (e) ANBO After Adsorption

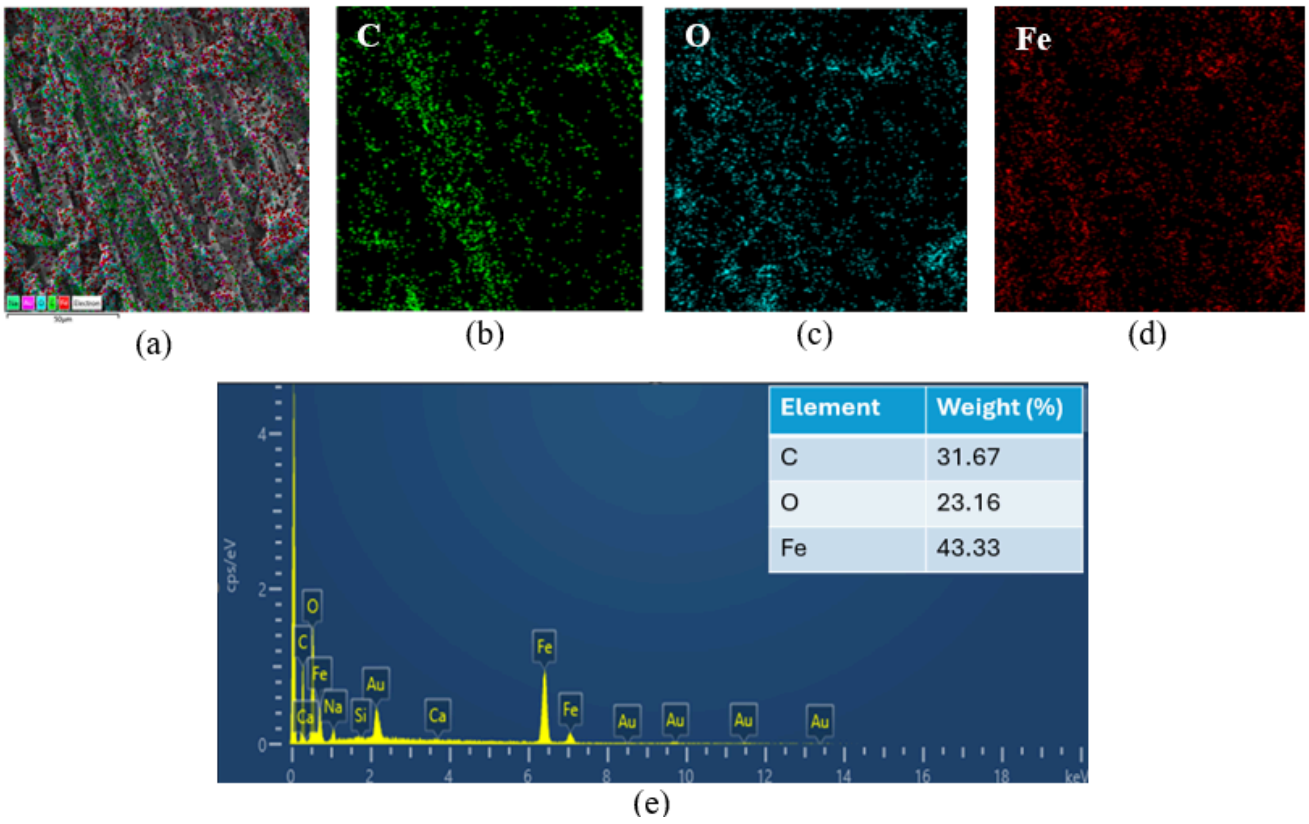

Figure 4

EDX analysis of (a) a selected image of ANBO prior to adsorption with matching mapping pictures for C, O, and Fe shown in (b), (c), and (d), respectively, and (e) the elemental spectra and composition.

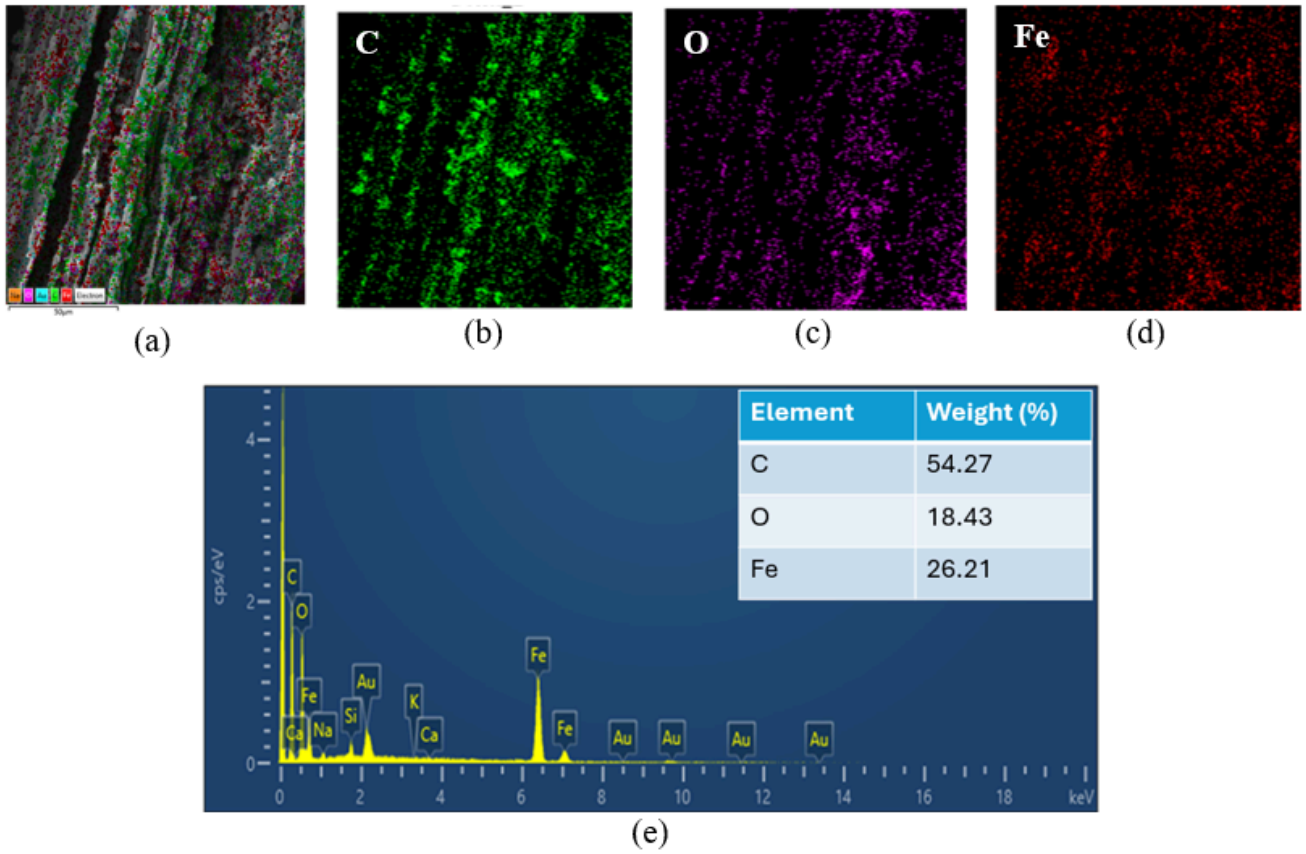

Figure 5

The EDX analysis of (a) a particular image of ANBO after adsorption, together with the associated mapping images for carbon, oxygen, and iron in (b), (c), and (d), respectively, and (e) the elemental spectra and composition of the ANBO sample

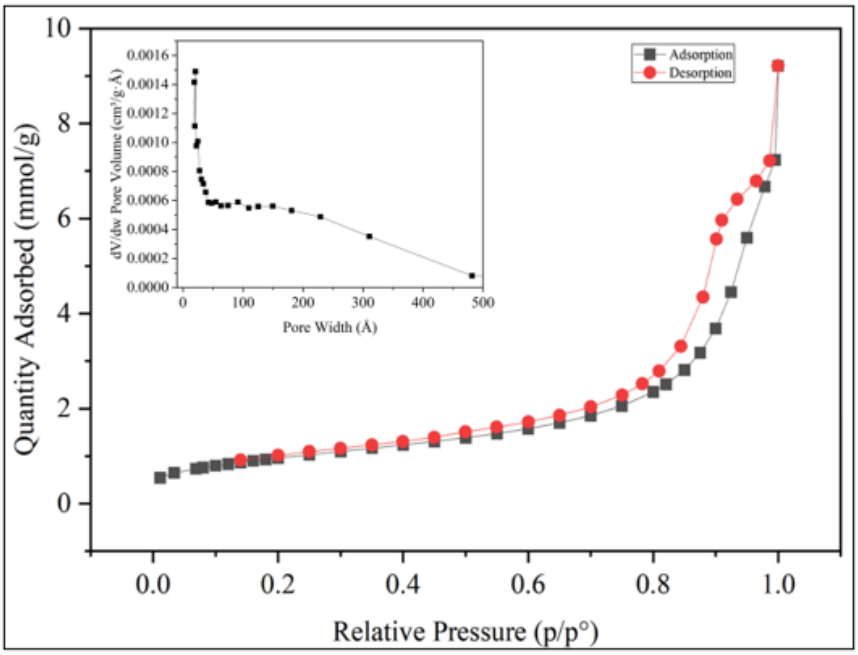

Figure 6

N_2 adsorption–desorption isotherms and BJH pore size distribution curves (inset) of ANBO

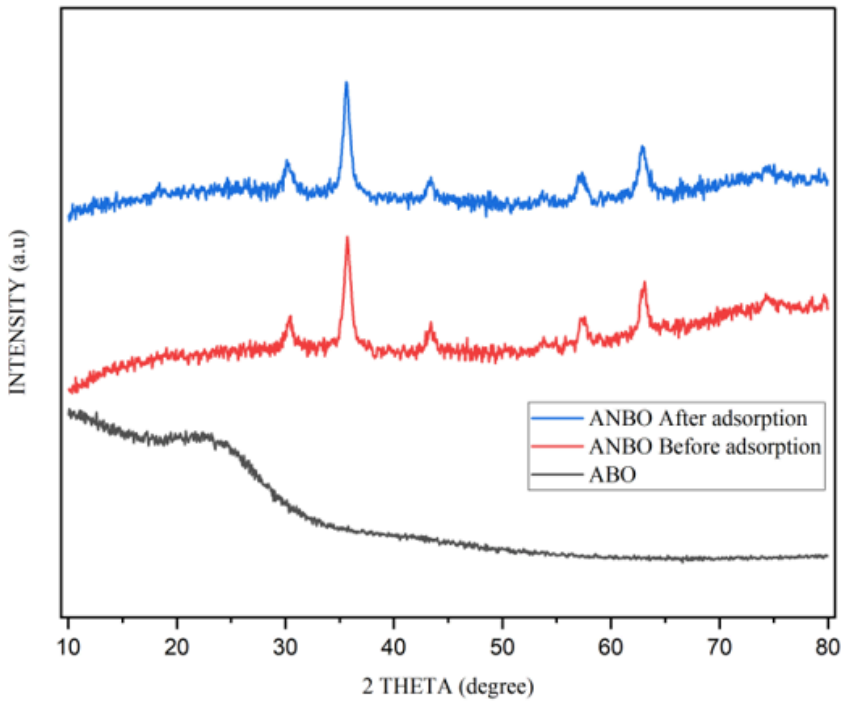

Figure 7

X-ray diffraction patterns before and after the adsorption of MG on ANBO and ABO

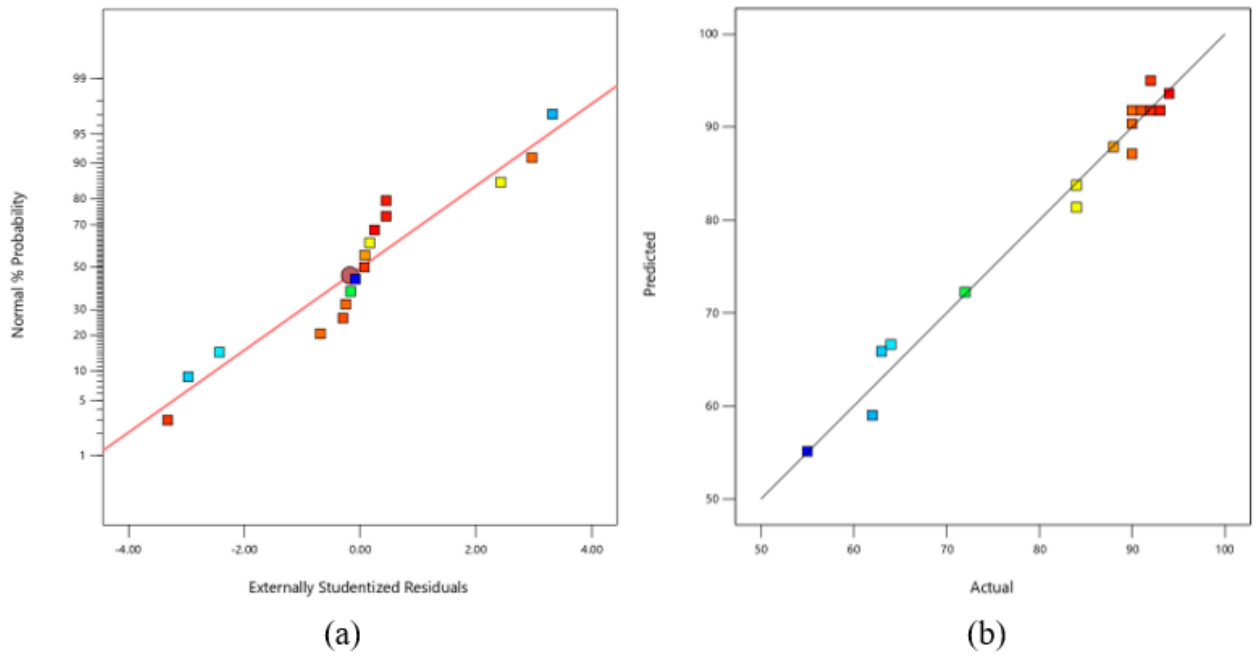

Figure 8

(a) Normal probability of residuals, and (b) predicted MG removal vs. actual MG removal via ANOVA.

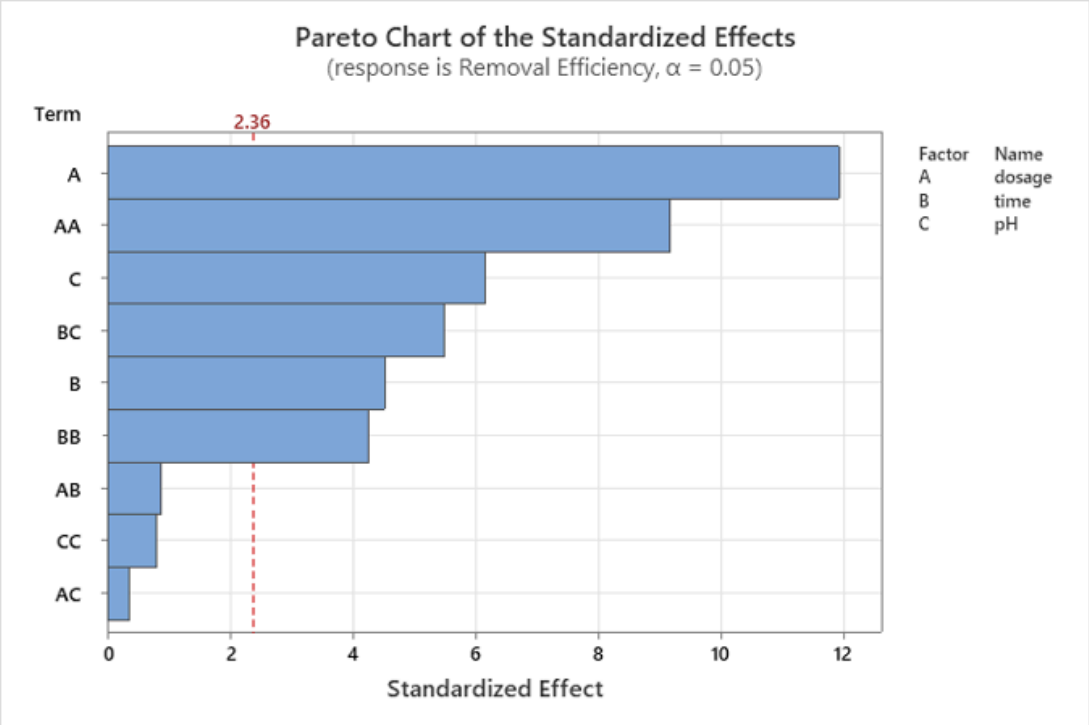

Figure 9

Pareto chart of standardized effects (response is %R) for MGs

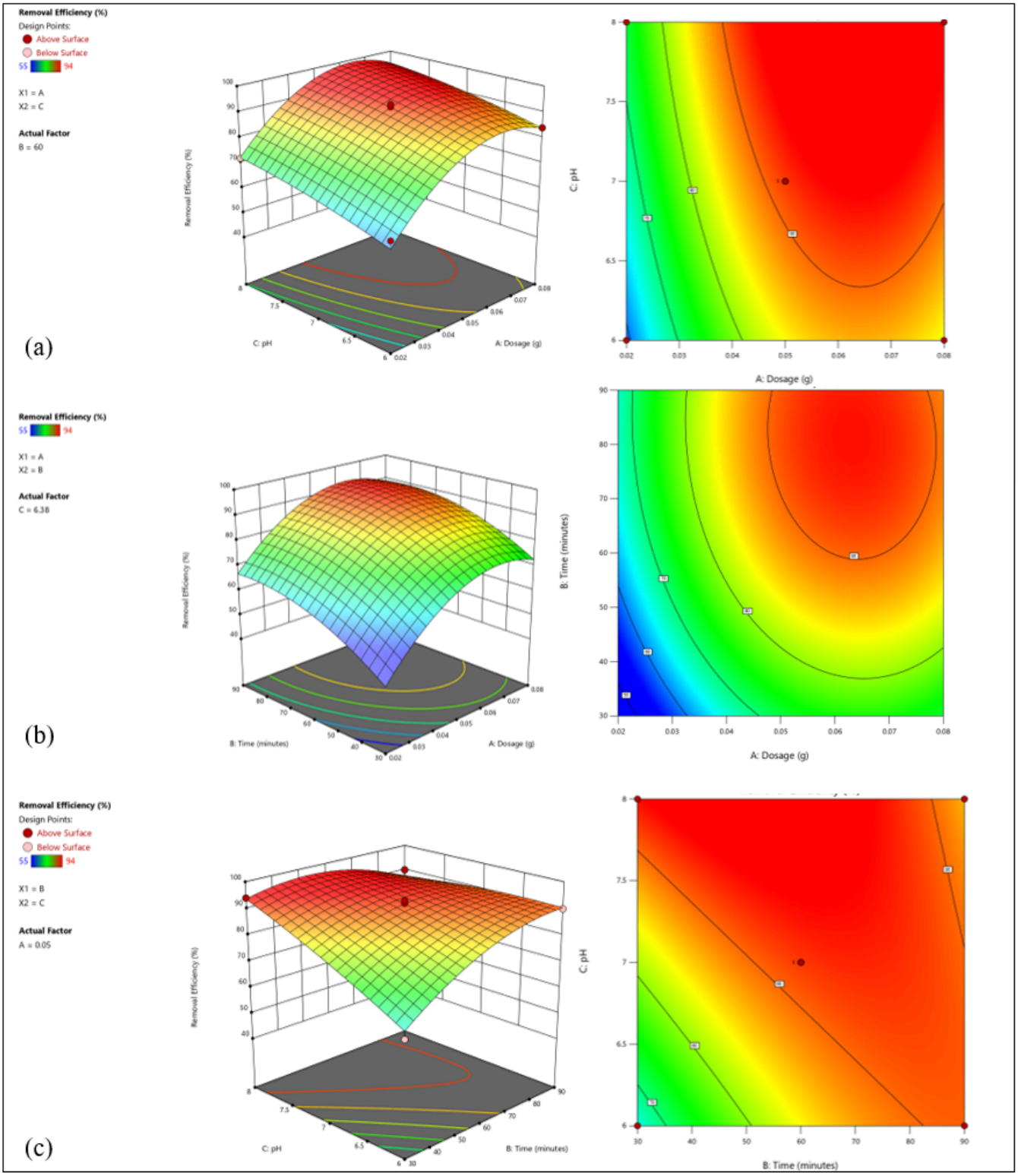

Figure 10

3D surface plot and 2D contour plot for the effects of (a) dosage and pH, (b) dosage and time, and (c) time and pH on the percentage of MG removed